The Thesis committee for Marshall Caleb Johnson

Certifies that this is the approved version of the following thesis:

Doppler Tomographic Observations of Exoplanetary Transits

APPROVED BY

SUPERVISING COMMITTEE:

Supervisor: _____

Sarah E. Dodson-Robinson

_____

William D. Cochran

Doppler Tomographic Observations of Exoplanetary Transits

by

Marshall Caleb Johnson, B.A.

Thesis

Presented to the Faculty of the Graduate School

of The University of Texas at Austin

in Partial Fulfillment

of the Requirements

for the Degree of

Master of Arts

The University of Texas at Austin

August 2013

Acknowledgments

Many thanks to my advisors, Bill Cochran and Sally Dodson-Robinson, and to the rest of my research committee–Mike Endl, Rob Robinson, and Chris Sneden–for helping guide me through this project. Thanks to Simon Albrecht for invaluable assistance in the development of the tomography code, and to Josh Winn for valuable discussions. I gratefully acknowledge funding from a NASA Earth and Space Science Fellowship under Grant NNX12AL59H. This work was also supported by NASA grant NNX11AC34G to WDC. This thesis includes data taken at The McDonald Observatory of The University of Texas at Austin. The Hobby-Eberly Telescope (HET) is a joint project of the University of Texas at Austin, the Pennsylvania State University, Stanford University, Ludwig-Maximilians-Universität München, and Georg-August-Universität Göttingen. The HET is named in honor of its principal benefactors, William P. Hobby and Robert E. Eberly.

Marshall Caleb Johnson

The University of Texas at Austin

August 2013

Doppler Tomographic Observations of Exoplanetary Transits

by

Marshall Caleb Johnson, M.A.
The University of Texas at Austin, 2013
SUPERVISOR: Sarah E. Dodson-Robinson

Transiting planet candidates around rapidly rotating stars, a number of which have been found by the *Kepler* mission, are not amenable to follow-up via the usual radial velocity techniques due to their rotationally broadened stellar lines. An alternative method is *Doppler tomography*. In this method, the distortions of the stellar spectral lines due to subtracted light during the transit are spectroscopically resolved. This allows us to not only validate the transiting planet candidate but also to obtain the spin-orbit misalignment for the system. The spin-orbit misalignment is a powerful statistical tracer of the migration histories of planets. I discuss our project to perform Doppler tomographic observations of *Kepler* candidates and other transiting planets using the facilities at McDonald Observatory. I present our first transit detection, that of Kepler-13 b, and discuss some other recent results.

Contents

Acknowledgments **iv**

Abstract **v**

Chapter 1 Introduction **1**

1.1 Scientific Background 1

1.2 Doppler Tomography 10

1.3 Kepler-13 b 17

Chapter 2 Methodology **22**

2.1 Observations 22

2.2 Line Profile Extraction 23

2.3 Transit Parameter Extraction 27

2.4 Testing the Code 30

Chapter 3 Results **33**

Chapter 4 Discussion **37**

Chapter 5 Conclusions **43**

5.1 Future Work 44

5.2 Sensitivity Estimation 48

Bibliography **55**

Chapter 1

Introduction

1.1 Scientific Background

The discovery of the first exoplanet orbiting a main-sequence star, 51 Peg b (Mayor & Queloz 1995), was surprising in part because of its extremely close orbit around its host star, a type of orbit not seen in our own solar system. Indeed, there quickly emerged a large population of massive planets on close orbits ($P \lesssim 5$ days) around their host stars, known as hot Jupiters. Although these planets are rare (as determined by Wright et al. 2012, 1.2%±0.38% of nearby FGK dwarfs host such planets), they are easy to find with both radial velocity and transit surveys, a fact first recognized by Struve (1952) but largely ignored until the discovery of 51 Peg b.

The discovery of hot Jupiters was surprising, in part, because it is thought that giant planets must form beyond the ice line, the location in a protoplanetary

disk where ice can condense and hasten grain growth (e.g., Lin et al. 1996; Bodenheimer et al. 2000). Thus, there must be some migration mechanism to move the planets from beyond the ice line to their current locations close to their host stars. Several mechanisms have been proposed for this; three of these are tidal interactions with the protoplanetary disk, planet-planet scattering, and Kozai cycles.

Tidal interactions with the protoplanetary disk were first considered in the context of planetary satellites by Goldreich & Tremaine (1980); a recent review is given by Kley & Nelson (2012). The planet's gravity stirs the disk, creating two tidal tails or spiral arms, one inside the planetary orbit and leading the protoplanet, the other outside and traling. The portions of these arms closest to the planet exert a gravitational torque on the planet. If there is an imbalance in the torques exerted on the planet by the two clumps, the planet will either gain angular momentum and spiral outwards or lose angular momentum and spiral inwards. The details of the imbalance, and thus the speed and direction of the migration, depend on the gradients within the disk and whether the planet is sufficiently massive enough to open a gap in the disk, but most plausible disk models result in inward migration.

In planet-planet scattering (e.g., Rasio & Ford 1996), systems of multiple closely-spaced giant planets form. The presence of the protoplanetary disk damps inclinations and eccentricities, but once the disk dissipates this damping cannot mitigate the effects of gravitational interactions between the planets. The system

becomes chaotic, and the planets may be emplaced onto highly eccentric orbits or ejected from the system altogether. If a planet is placed on such a highly eccentric orbit with a small pericenter, it will undergo tidal damping during pericenter passages and eventually become a hot Jupiter on a short period, circular orbit about its host star.

Another possible mechanism is Kozai cycles plus tidal friction (KCTF; Fabrycky & Tremaine 2007). Kozai cycles rely on the presence of a distant, massive perturbing body, either a second planet or a stellar companion, on an inclined orbit. If the initial inclination between the orbital planes of the planet and perturber is greater than $i_{crit} = 39.2°$, then the gravity of the perturber will be able to torque the planet's orbit. This results in a complex orbital evolution wherein the eccentricity and inclination of the planet's orbit oscillate on timescales short compared to the age of the system. If the precession timescale is much longer than the orbital timescale of either the inner or outer binary, then the semimajor axes of both binaries will be conserved. Like for planet-planet scattering, this can place the planet on a highly eccentric orbit with a small pericenter, and the subsequent tidal damping leaves the planet on a highly inclined, circular orbit around its host star.

Observations over the past years have shown the orbits of many of these short-period giant planets are highly misaligned with respect to their host stars' spin axes (e.g., Triaud et al. 2010; Winn et al. 2011). This was initially surprising, given

that planets are thought to form in protoplanetary disks that are expected to be well-aligned with their stars' equators. However, all of the planets for which the spin-orbit misalignment has been measured to date are short-period giant planets, where the migration mechanisms discussed above must have operated. While migration through tidal interactions with the disk is expected to leave the planets on aligned orbits, both planet-planet scattering and Kozai cycles are expected to produce broad distributions of spin-orbit misalignments.

Once a statistically significant sample of spin-orbit misalignments had been collected, a pattern emerged. Winn et al. (2010) note that planets (at the time, the sample consisted almost entirely of hot Jupiters) orbiting cooler stars ($T_{eff} <$ 6250 K) are predominantly aligned, while those around hotter stars ($T_{eff} >$ 6250 K) have a broad spin-orbit misalignment distribution; indeed, this distribution is consistent with isotropic (Albrecht et al. 2012). Winn et al. (2010) hypothesized that this bimodal distribution is due to the properties of the host stars. Below 6250 K, stars have deep convective zones, resulting in efficient tidal damping; a population of initially inclined planets will quickly become aligned. Above 6250 K, however, the convective zones have become thin and have a sufficiently small mass that they cannot efficiently align misaligned planets; an initially inclined population will remain misaligned. Further work (Albrecht et al. 2012) supports, but has not yet confirmed, this hypothesis. Additionally, the large number of multiplanet systems

discovered by *Kepler* has allowed the measurements of spin-orbit misalignments for a number of compact multiplanet systems; while the sample is still small ($N = 5$), all are aligned, suggesting that these systems likely undergo only quiescent disk migration, rather than disruptive planet-planet scattering (Albrecht et al. 2013b). Kozai cycles in such strongly interacting systems can cause the orbital plane of the planetary system as a whole to precess (e.g., Kaib et al. 2011) but will not result in significant migration.

An alternate hypothesis was presented by Rogers et al. (2012). They performed simulations of the redistribution of angular momentum by gravity waves within hot stars, which suggest that this redistribution can cause large changes in the rotational properties of the outer layers of the star on short timescales. That is, the rotation of the stellar atmosphere–the visible portion of the star–would not reflect the bulk rotation of the star. Thus, an initially aligned population of planets would *appear* to be misaligned, even if the total stellar angular momentum and planetary orbital angular momentum vectors were aligned. There are several possible tests of this hypothesis; perhaps the most definitive would be a test of the prediction that compact multiplanet systems around hot stars should be as misaligned as hot Jupiters around such stars. The five multi-planet transiting systems considered by Albrecht et al. (2013b) all have host stars with temperatures either less than 6250 K or differing from 6250 K by $< 1\sigma$ and so do not provide a good test of this

hypothesis.

Rogers & Lin (2013) model the tidal realignment of an initially misaligned population of hot Jupiters, under the assumption that the tidal realignment timescale must be much smaller than the tidal orbital decay timescale in order to preserve the population of hot Jupiters. They find that under these conditions, the planets around slowly-rotating (prediminantly cool) stars do not uniformly migrate to zero obliquity, but rather to obliquities around zero, $\pm 90^\circ$, and 180°, inconsistent with the observations detailed above. This, they suggest, is consistent with migration predominantly through tidal interactions with the protoplanetary disk, and the subsequent realignment of the stars' outer layers proposed by Rogers et al. (2012).

A third hypothesis for the origin of the spin-orbit misalignment distribution has been put forward by Batygin (2012). They propose, using analytical models, that during the star formation process some fraction of stars are members of transient binary systems that are later disrupted by interactions in protostellar clusters. If the orbits of these transient binary systems are misaligned with respect to the protoplanetary disk around one of the stars (for transiently captured companions the distribution is expected to be isotropic), then the disk will be torqued and can end up in an orbit misaligned with respect to the stellar spin. If this occurs, disk migration can result in a population of misaligned systems. Misaligned planets around cool stars would have their inclinations tidally damped, as in the Winn et al. (2010)

hypothesis. Batygin (2012) also argue that disk misalignment could result simply from the stellar orbit around the protocluster, if the disk is initially inclined with repect to this orbit. The critical test of this hypothesis is that it predicts that some fraction of compact multiplanet systems around both cool and hot stars should be misaligned.

On the other hand, Dawson & Murray-Clay (2013) have presented evidence that planet-planet scattering does operate in a significant number of systems. They considered the sample of radial velocity-detected giant planets with periods of 10 days $< P <$ 100 days, which should have undergone significant migration but should not have undergone significant tidal damping. They found that, in this sample of planets, those with eccentric orbits are preferentially found around metal-rich stars; due to the well-established planet-metallicity correlation (e.g., Fischer & Valenti 2005), these stars would be expected to be more likely to form the systems of multiple closely-spaced giant planets that are the initial conditions for planet-planet scattering. Dawson & Murray-Clay (2013) also found that those hot Jupiters that still retain some orbital eccentricity–expected to be planets that have been emplaced via planet-planet scattering (or Kozai cycles) but have not yet had their orbital eccentricity damped out–are also preferentially found around metal-rich stars. An additional test of the importance of planet-planet scattering will be to gather a sample of spin-orbit misalignment measurements for planets in this period range;

currently, all of the planets in this period range with such measurements are in the compact multiplanet systems discussed above (Albrecht et al. 2013b).

The tension between the results presented by and the hypotheses of Dawson & Murray-Clay (2013), Albrecht et al. (2012) and Winn et al. (2010) versus those of Rogers et al. (2012) and Rogers & Lin (2013) versus that of Batygin (2012) highlights the importance of expanding the parameters space of planets with measurements of the spin-orbit misalignment. To date the vast majority of planets with measured spin-orbit misalignments are hot Jupiters, with a few planets in compact multiplanet systems. The different hypotheses can be tested by obtaining spin-orbit misalignment measurements for a statistically significant sample of planets with longer periods, and in multi-planet systems around hot stars. Specifically, the three hypotheses make the following predictions.

Winn et al. (2010) hypothesize that the spin-orbit misalignment distribution is the result of emplacement of an initially misaligned population, followed by tidal damping of planets around cool stars. Tidal damping, however, is strongly dependent on the semmajor axis. Thus, under this hypothesis, we would expect that planets around cool stars with orbits sufficiently long to prevent significant tidal damping within the main sequence lifetime of the host star would show a similar degree of misalignment to hot Jupiters around hot stars. Gas giant planets in this period range will be the most favorable targets for this work, as their large radii

make them amenable to Doppler tomographic observations (see Chapter 1.2).

Under the Rogers et al. (2012) hypothesis, it is the host stars themselves that are misaligned, not the planetary orbits. Thus, a strong test of this hypothesis would be to observe compact multiplanet systems around hot stars. It is expected that these systems must have formed via disk migration, as the more violent processes of planet-planet scattering or Kozai cycles would have disrupted these systems. The Rogers et al. (2012) hypothesis thus predicts that these compact multiplanet systems should show a similar degree of misalignment as the hot Jupiters around these stars.

Compact multiplanet systems will also provide a crucial test of the Batygin (2012) hypothesis. Under this hypothesis, hot Jupiters are produced by disk migration within misaligned disks; therefore, there should be misaligned compact multplanet systems around both hot stars and cool stars (as long as the planets in the latter class of systems have sufficiently small masses or sufficiently long orbital periods to avoid tidal damping; the tidal damping timescale is inversely proportional to both planetary mass and semimajor axis).

Some care must be taken, however, in the interpretation of any misaligned compact multiplanet systems that are discovered. Kaib et al. (2011) simulate Kozai cycles in the 55 Cnc system, which contains five planets on short-period orbits (and thus is a compact multiplanet system) as well as a distant stellar companion. In such as system, with gravitational interactions between the planets, Kozai cycles

manifest not as eccentricity and inclination variations of a single planet but rather as precession of the orbital plane of the planetary system.

Observations of the spin-orbit misalignments of a statistically significant sample of longer-period planets and planets in compact multiplanet systems is thus critical to distinguishing between the competing hypotheses described above. In the next section I will describe how I am contributing to the collection of this sample of measurements. Observations of a larger sample of hot Jupiters, however, continues to be important–not only to further solidify the statistics, but also to identify systems which do not follow the pattern identified by Winn et al. (2010). Indeed, it is the three original systems around cool stars with misaligned orbits–HD 80606 b, WASP-8 b, and HAT-P-11 b–that directly contributed to the formation of the Winn et al. (2010) hypothesis, as all of these systems have long tidal damping timescales due to either long-period orbits or small planetary mass.

1.2 Doppler Tomography

The vast majority of the measurements of the spin-orbit misalignments of transiting exoplanets have come via the Rossiter-McLaughlin effect. In this work I use Doppler tomography, a related technique. I will now discuss these methods of observation.

When an object transits a rotating star, it will successively block regions of the stellar disk with different radial velocities. It has long been recognized that this

will cause a distortion of the spectral lines (Rossiter 1924; McLaughlin 1924) due to the subtracted light.

Observationally, this can manifest in two different manners. For low stellar rotational velocities (compared to the intrinsic stellar linewidth), this is most easily observed as an apparent shift in the radial velocity of the lines because of the line asymmetry. The manner in which this shift occurs gives the spin-orbit misalignment λ: a prograde planet will first block the approaching hemisphere of the star and then the receding hemisphere, and thus the velocities will become first positive and then negative; the opposite will be seen for a retrograde planet. This is accomplished by observing the star during the transit using a high resolution spectrograph and an iodine absorption cell, such as is used for radial velocity planet search programs. This has been the primary method for determining the spin-orbit misalignment of exoplanets (e.g., Triaud et al. 2010; Winn et al. 2011).

If, however, the star is sufficiently rapidly rotating ($v \sin i \gtrsim 5 - 10$ km s^{-1}, depending on the spectrograph resolution), the spectral line distortions can be *directly* resolved. This technique is known as *Doppler tomography*, as it maps the time series spectral line distortions to a time-series one-dimensional map of the stellar surface and any obscurations (i.e., transiting planets). For even more rapidly rotating stars ($v \sin i \gtrsim 30$ km s^{-1}; A. Collier Cameron, personal communication), the subtracted light manifests as a discrete "bump" that moves across the line profile,

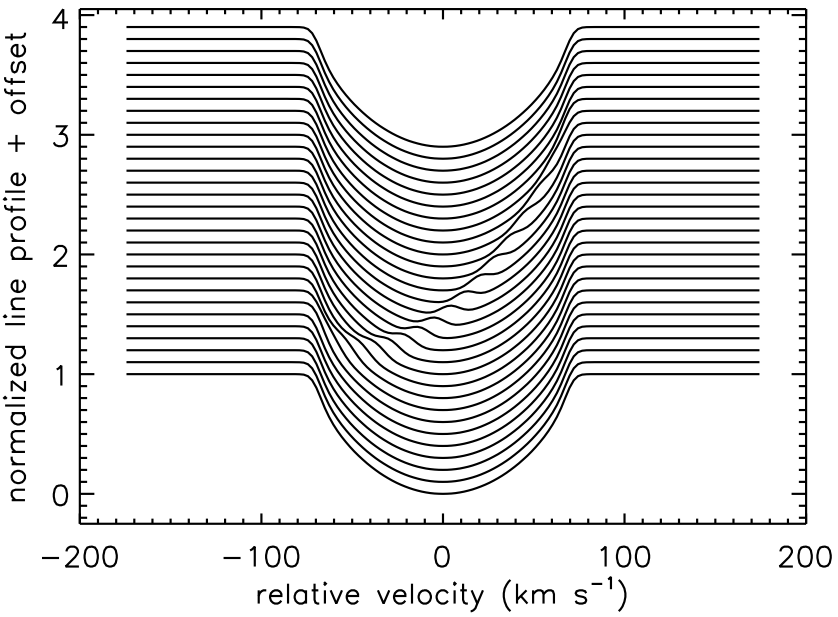

Figure 1.1 Model line profiles during a transit, showing the distortion due to the planetary shadow moving across the absorption line. Each consecutive line profile is displaced upwards by an arbitrary amount for display purposes; time increases from bottom to top. The model was produced using the code destribed in Chapter 2.3, using a planet with $R_p/R_* = 0.09$ orbiting a star with $v \sin i = 70$ km s^{-1} with spin-orbit misalignment $\lambda = 0^\circ$ and impact parameter $b = 0$.

rather than an overall distortion of the line profile. See Fig. 1.1 for an illustration of this effect.

The manner in which the distortion moves across the line profile maps directly to the path of the planet across the stellar disk. The most critical parameters for this path are the afforementioned spin-orbit misalignment λ and the impact parameter $b = a/R_* \cos i$, where a is the planet's semimajor axis, R_* is the stellar radius, and i

is the angle between the normal to the planetary orbital plane and the line of sight. b is thus the minimum projected distance between the center of the stellar disk and the center of the planetary disk during the transit, in units of the stellar radius. I note that the spin-orbit misalignment λ is not the full three-dimensional planetary obliquity, but rather this obliquity projected onto the plane of the sky. The other parameters that affect the time series line profiles are the planetary orbital period, time of center of transit, and the planetary-stellar radius ratio R_p/R_*, which sets the width and height of the line profile perturbation, all of which are typically best determined from photometry, which usually has better time resolution than the spectroscopic data, and the stellar line width, set by $v \sin i$, where here i is the angle between the stellar rotation axis and the line of sight, determined from spectroscopy.

The data are typically displayed not as the time series line profiles shown in Fig. 1.1 but rather as a grayscale map after the average line profile has been subtracted off; these are referred to as the *time series line profile residuals*. Here the planetary transit signature manifests as a bright linear streak across the line profile. This is illustrated in Fig. 1.2, where model time series line profile residuals are shown for a variety of values of λ. Note how the differing values of λ change the slope of the line denoting the planetary transit signature. In Fig. 1.3 I display planetary transit signatures for different values of b; note how increasing values of b result in the transit signature crossing a smaller range of velocities, as the planetary

transit chord across the stellar disk is also shorter. The transit duration, for a fixed orbital period, is also shorter for larger impact parameters. Thus knowledge of the orbital period allows us to break a potential degeneracy between b and λ–compare the panels in Fig. 1.2 ($\lambda = 45°$, $b = 0$) and Fig. 1.3 ($\lambda = 0°$, $b = 0.7$); while visually similar, the transit with the non-zero impact parameter is notably shorter.

The magnitude and observability of the line profile distortion is influenced by several parameters. The width of the line profile perturbation is set by $v \sin i$ and the transit depth (i.e., R_p/R_*), while the overall amount of subtracted light is set by R_p/R_*. Targets with large $v \sin i$ and large R_p/R_* are more favorable. Additionally, the noise level in a given spectrum is set by the amount of flux received during an exposure; thus, the target star brightness also influences observability. Obviously, brighter targets are more favorable than fainter ones.

Doppler tomography can be used to validate transiting planet candidates around rapidly-rotating stars. With significantly rotationally broadened spectral lines, these stars are not amenable to follow-up using high precision radial velocity observations. However, detection of the Doppler tomographic transit signature allows us to verify that the transiting object is indeed orbiting the expected star, i.e., that the system is not a background eclipsing binary star blended with a brighter foreground star. By examining the line shape we can also rule out scenarios where the transiting object is another star, as we will be able to see an additional set of

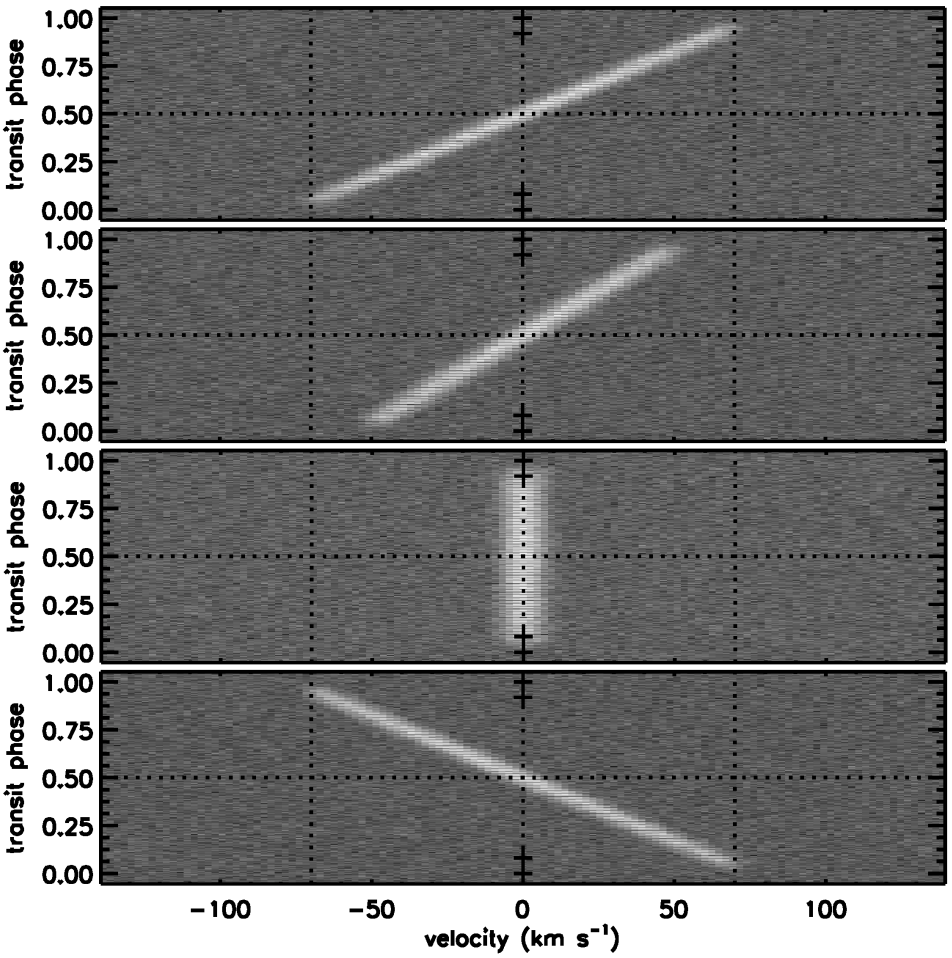

Figure 1.2 Model time series line profile residuals for planets with the same parameters as in Fig. 1.1, except with, from top to bottom, $\lambda = 0°$, $\lambda = 45°$, $\lambda = 90°$, and $\lambda = 180°$. A small amount of artificial noise has been added to better approximate actual data. Time increases from bottom to top in each panel. Vertical lines mark $v = 0, \pm v \sin i$, and a horizontal dashed line marks the time of mid-transit. Small crosses mark the times of first, second, third and fourth contacts. Transit phase is defined such that ingress=0 and egress=1.

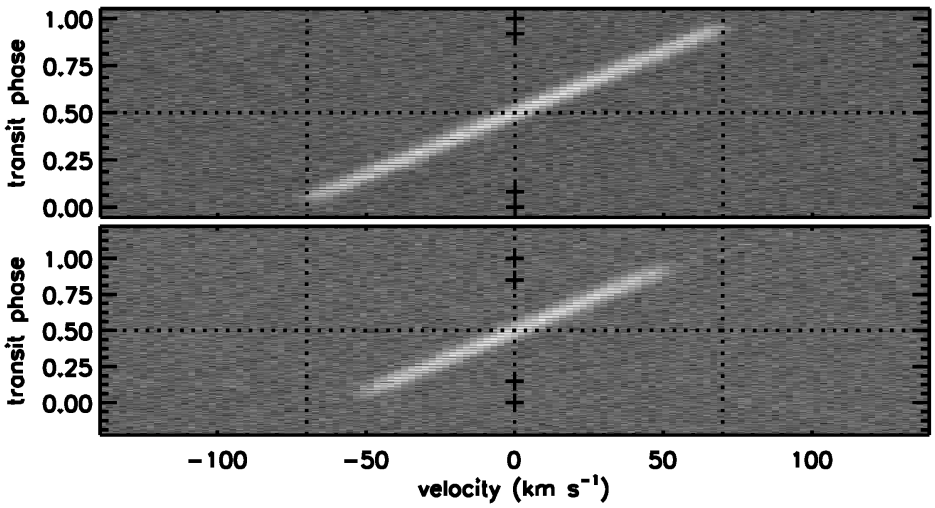

Figure 1.3 Model time series line profile residuals for planets with the same parameters as in Fig. 1.1, except with $b = 0$ (top) and $b = 0.7$ (bottom). A small amount of artificial noise has been added to better approximate actual data. Notation on the figure is the same as in Fig. 1.2.

absorption lines superposed upon those of the primary. The limitation, however, is that Doppler tomography cannot measure the mass of the transiting object, and thus we cannot, for example, distinguish between a hot Jupiter, a brown dwarf, and a small M dwarf, all of which have similar radii and the latter of which would, in many cases, have an insufficient flux ratio to make a detectable imprint upon the spectrum of the primary.

The technique of Doppler tomography (also known as *Doppler imaging* or *line-profile tomography*) was originally developed to map starspots on rapidly-rotating stars (Vogt & Penrod 1983). It has since been applied to eclipsing binary stars (e.g., Albrecht et al. 2013a), transiting planets (which I will briefly summarize), and stellar

non-radial oscillations (e.g., Gies & Kullavanijaya 1988).

The first applications to exoplanets were to the planet WASP-33 b (Collier Cameron et al. 2010b, to date still the only planet confirmed with Doppler tomography), and to the well-known transiting planet HD 189733 b (Collier Cameron et al. 2010a). Since this time, all of the published Doppler tomographic observations have been of confirmed planets, and moreover have been reanalyses of conventional Rossiter-McLaughlin data: for WASP-3 b (Miller et al. 2010), CoRoT-11 b (Gandolfi et al. 2012), KOI-94 b (Albrecht et al. 2013b), and WASP-32 b and WASP-38 b (Brown et al. 2012).

We have instituted a program of observations at McDonald Observatory to use Doppler tomography to confirm *Kepler* planet candidates around rapidly-rotating host stars, and also to determine spin-orbit misalignments for planets discovered by ground-based transiting surveys. Here we present our first results, on the *Kepler* planet Kepler-13 b.

1.3 Kepler-13 b

Kepler-13 is distinguished as the hottest star known to host a transiting planet (at $T_{eff} = 8500 \pm 400$ K), and the second-hottest star with a known planet (second only to κ And, $T_{eff} = 10700$ K, host to a widely-separated "super-Jupiter" discovered by direct imaging; Carson et al. 2013). Stellar parameters for Kepler-13 are given

in Table 1.1. As Kepler-13 b (aka KOI-13 b, KOI-13.01) is a hot Jupiter, it is one of the hottest known planets; Mazeh et al. (2012) estimate $T_{eff} = 2600 \pm 150$ K using the secondary eclipse depth in the *Kepler* passband.

The planet Kepler-13 b was originally confirmed by Barnes et al. (2011) through detection of a gravity-darkening signature in the transit lightcurve from *Kepler*. This also enabled them to measure the spin-orbit misalignment, albeit with degeneracies, to be $\lambda = \pm 24 \pm 4^\circ$ or $\lambda = \pm 156 \pm 4^\circ$. Shporer et al. (2011), Mazeh et al. (2012), Mislis & Hodgkin (2012), and Esteves et al. (2013) detect beaming and ellipsoidal variations from the planet, and use these to measure the mass of Kepler-13 b to be $\sim 8 - 10 M_J$, putting it firmly within the planetary regime. Many of these different authors, however, found conflicting values for some of the transit and system parameters, especially the impact parameter b (see Table 1.2).

The Kepler-13 (aka KOI-13, BD+46 2629) system has long been known to be a proper motion binary (Aitken 1904). Szabó et al. (2011) determined that it consists of two A-type stars with similar properties (see Table 1.1). They also determined that the transiting planet Kepler-13 b orbits the brighter of the two binary components, Kepler-13 A. Despite the resulting blend, as the separation between Kepler-13 A and B is much smaller than the size of one of *Kepler*'s pixels, the inferred radius for Kepler-13 b remains in the planetary range, albeit at the highly-inflated end of that range. This, however, is unsurprising considering the luminous

host star and close orbital proximity of the planet to the star, and consequently high planetary temperature. Santerne et al. (2012) detected a third stellar component in the system. They determined that this companion, Kepler-13 Bb, with a mass of $0.4M_{\odot} < M < 1M_{\odot}$, orbits Kepler-13 B with a period of 65.8 days on a highly eccentric orbit. Kepler-13 b thus orbits one member of a stellar triple system, or, considering the massive planet Kepler-13 b, a heirarchical quadruple system. The properties of the stars are summarized in Table 1.1.

Kepler-13 A is rapidly rotating ($v \sin i = 76.6$ km s^{-1}; Santerne et al. 2012) and bright for a *Kepler* target ($Kp = 9.96$), making it an excellent target for Doppler tomography.

Table 1.1. Previous State of Knowledge about the Stellar Components of the Kepler-13 System

Parameter	Santerne et al. (2012)	Szabó et al. (2011)
System Parameters		
d (pc)	-	500
age (Gyr)	-	$0.708^{+0.183}_{-0.146}$
A_V (mag)	-	0.34
Kepler-13 A		
V (mag)	-	9.9
T_{eff} (K)	-	8511^{+401}_{-383}
$\log g$ (cgs)	-	3.9 ± 0.1
[Fe/H]	-	0.2
$v \sin i$ (km s^{-1})	76.6 ± 0.2	65 ± 10
$M_*(M_\odot)$	-	2.05
$R_*(R_\odot)$	-	2.55
Kepler-13 B		
V (mag)	-	10.2
T_{eff} (K)	-	8222^{+388}_{-370}
$\log g$ (cgs)	-	4.0 ± 0.1
[Fe/H]	-	0.2
$v \sin i$ (km s^{-1})	62.7 ± 0.2	70 ± 10
$M_*(M_\odot)$	-	1.95
$R_*(R_\odot)$	-	2.38
Kepler-13 Bb	-	-
P (days)	65.831 ± 0.029	-
e	0.52 ± 0.02	-
K (km s^{-1})	12.42 ± 0.42	-
$M_*(M_\odot)$	$> 0.4, < 1$	-

Note. — K is the radial velocity semi-amplitude of Kepler-13 B due to its mutual orbit about Kepler-13 Bb.

Table 1.2. Previous State of Knowledge about Kepler-13 b

Parameter	Esteves et al. (2013)	Mazeh et al. (2012)	Mislis & Hodgkin (2012)	Szabó et al. (2012)	Shporer et al. (2011)	Barnes et al. (2011)	Szabó et al. (2011)
R_p (R_J)	2.042 ± 0.080	-	-	-	-	1.393 ± 0.015	2.2 ± 0.1
M_p (M_J)	7.95 ± 0.27	10 ± 2	8.3 ± 1.25	9.2 ± 1.1	-	-	-
P (days)	-	-	-	-	1.7637 ± 0.0013	-	-
b	$0.3681^{+0.0041}_{-0.0064}$	0.75 ± 0.01	-	0.253 ± 0.020	-	0.31962	0.75
λ (°)	-	-	-	-	-	$\pm 24 \pm 4$ or $\pm 156 \pm 4$	-
ψ (°)	-	-	-	-	-	-45 ± 4	-
ϕ (°)	-	-	-	-	-	54 ± 4	-
i (°)	$85.135^{+0.09}_{-0.063}$	-	-	-	-	85.9 ± 0.4	-
a/R_*	$4.3396^{+0.0102}_{-0.0075}$	3.17 ± 0.06	-	-	-	-	
R_P/R_*	$0.080509^{+0.000033}_{-0.000048}$	0.0907 ± 0.0005	-	-	-	0.084508	0.0884 ± 0.0027
$P_{rot,*}$ (hr)	-	-	-	23.45 ± 0.05	-	22.5	-
f_*	-	-	-	-	-	0.018	-

Note. — Values from Barnes et al. (2011) assume a value of $M_* = 1.83 M_\odot$. b is the impact parameter, λ is the projection of the spin-orbit misalignment onto the plane of the sky, ψ is the stellar obliquity, ϕ is the full three-dimensional spin-orbit misalignment, and $f_* = (R_{eq} - R_{pole})/R_{eq}$ is the stellar dynamical oblateness (Barnes 2009), where R_{eq} and R_{pole} are the stellar equatorial and polar radii, respectively.

Chapter 2

Methodology

2.1 Observations

Observations of Kepler-13 b were taken with two telescopes located at McDonald Observatory, the 9.2m Hobby-Eberly Telescope (HET) and the 2.7m Harlan J. Smith Telescope (HJST). The HET utilizes a fiber-fed spectrograph, the High-Resolution Spectrograph (HRS; Tull 1998). The fibers have a diameter of 2", and so our observations include blended light from both Kepler-13 A and B. The Robert G. Tull Spectrograph (TS23) on the HJST, on the other hand, is a more traditional slit Coudé spectrograph. There is no facility to correct for image rotation, and so the relative contributions to the spectrum from Kepler-13 A and B vary throughout the course of an observation. Observations are summarized in Table 2.1. Our HRS observations were taken with a resolution $R = 30,000$, while the TS23 observations

Table 2.1. Transit Observations of Kepler-13 b

Date (UT)	Telescope	Transit Phases Observed
2011 Jun 8	HET	$0.65 - 0.98$
2011 Jun 15	HJST	$-0.12 - 1.25$
2011 Jul 6	HET	$0.03 - 0.48$
2011 Jul 8	HET	$0.10 - 0.51$
2011 Aug 21	HET	$0.21 - 0.66$
2011 Sep 13	HET	$0.29 - 0.71$
2011 Nov 5	HET	$-0.09 - 0.32$
2011 Nov 5	HJST	$-0.08 - 0.85$
2012 Jun 7	HET	$0.10 - 0.60$

Note. — I define transit phases such that ingress= 0 and egress= 1.

have $R = 60,000$.

Data reduction is performed using the same IRAF pipeline utilized by the McDonald Observatory Radial Velocity Planet Search Program. The data are blaze-divided, and any residual curvature is dealt with by fitting a second-order polynomial using a σ-clipping routine and normalizing.

2.2 Line Profile Extraction

The first step of our analysis is to extract the time series line profiles from the data. In order to accomplish this, we use the least squares deconvolution method of Donati et al. (1997). In this method, a model spectrum is produced by convolving a model

line profile with a set of appropriately-weighted delta functions at the locations of the spectral lines. We fit this model to the data using the nonlinear least squares method of Markwardt (2009) as implemented in the IDL function MPFIT and derivatives.

Our fitting proceeds in several steps, as follows.

First, we fit the telluric spectrum in several orders with many telluric lines, leaving only the telluric velocity as a free parameter. We assume that this fixes the spectrograph frame ($\pm$ the wind speed, which is much smaller than the velocity scales of interest to us). These velocities are then corrected to the solar barycentric frame, and the spectra are shifted into this frame.

Now that all spectra have been fixed to the solar barycentric frame, we stack all of the spectra from each individual night of observations in order to create nightly template spectra. We fit each nightly template using the least squares deconvolution method, leaving the stellar velocity as a free parameter. A theoretical rotationally broadened line profile (taken from Gray 2005), with $v \sin i$ fixed at the literature value, is used for the line shape. The line depths are fixed at values from the Vienna Atomic Line Database (VALD; Kupka et al. 2000). We thus correct each spectrum to the stellar barycenric frame (neglecting any acceleration of the star over the course of set of observations, typically $\sim 1 - 2$ hours).

All of the spectra, now in the stellar barycentric frame, are stacked to create a template spectrum. We now perform a differential normalization, fitting a

second-order function to the ratio between each order of each spectrum and the corresponding order of the template spectrum, and divide this out of each spectrum. This ensures that each spectrum has the same normalization as the template. The template is fit using least-squares deconvolution, but now the velocity is fixed at zero and the line depths are left as free parameters. The VALD line depths are used as the starting values. The line shape is again a theoretical rotationally broadened profile.

Finally, now that we have obtained best-fit line depths, we again use the least-squares deconvolution method, but now leave each pixel of the line shape as the free parameter, fixing the line depths and velocity offset. From this we get the average line profile for each order. These are regridded to a common velocity scale and combined using a weighted mean to obtain the average line profile from each spectrum. The line profile from each order is weighted by the signal-to-noise ratio at the center of that order multiplied by the total equivalent width of all modeled lines in that order, after Albrecht et al. (2013b). I also apply limits to the root-mean-squared noise of each line profile outside the profile wings in order to reject excessively noisy profiles.

What is of interest is, strictly speaking, not the line profiles but the time series line profile residuals, once the average line profile has been subtracted off. The average line profile is computed by averaging together all of the out-of-transit

line profiles, or, if there are not enough of these available, all of the line profiles. My code alternatively allows the subtraction of a theoretical rotationally broadened line profile; however, this typically gives poorer results due to systematic mismatches between the theoretical and observed line profiles.

2.2.1 Line Depths

One problem is that the values of the line depth calculated by VALD and used as initial guesses by my code are sometimes not a good fit to the data, to the extent that the code fails to fit a good line depth. Additionally, there are some lines that are simply not included in the models, either because they are rejected by the code because the line depths calculated by VALD are much smaller than those actually observed or because the lines does not appear in the VALD line list.

In these cases, I use the following approach. I identify this line in a high-resolution, high signal-to-noise solar spectrum, and measure its equivalent width. I then use MOOG (Sneden et al. 2012) to calculate the abundance implied by this line. The most uncertain parameter for a given line is its oscillator strength $\log(gf)$, and so I perform a differential analysis by fixing the expected abundance at the solar value (Asplund et al. 2009) and varying $\log(gf)$ until the abundance calculated by MOOG matches the solar value. In order to find the expected depth of the line for input to my least squares deconvolution code, I run MOOG again using the

ewfind driver and a Kurusz model stellar atmosphere calculated with parameters appropriate for my target transit host star. This gives a value for the expected equivalent width for the line in this star's spectrum. In order to convert this to an expected zero-rotational-broadening line depth, I assume that the baseline line shape is a Gaussian with width σ and depth D, centered at $v = 0$. The equivalent width will be (in velocity units)

$$W_v = \int_{-\infty}^{\infty} De^{-v^2/2\sigma^2} dv = D\sqrt{2\sigma^2\pi} \tag{2.1}$$

therefore, the line depth is

$$D = \frac{1}{\sigma\sqrt{2\pi}} W_v \tag{2.2}$$

Thus I calculate a better initial guess for the line depth.

2.3 Transit Parameter Extraction

Now that the time series line profile residuals have been computed, I must extract the transit parameters from these data.

I numerically compute a model for the time series line profile residuals and fit this to the data. The model is constructed by numerically integrating over the stellar disk, summing the contributions from each surface element to the overall line profile. A Gaussian line profile is assumed for each surface element; these are

then appropriately Doppler shifted, assuming solid body rotation, and scaled by a quadratic limb-darkening law. Cartesian coordinates are utilized for the integration and subsequent computations.

In order to improve computational efficiency, I do not perform the full integration for each exposure. Instead, I take the following approach. I compute the out-of-transit line profile. Then, we compute the location of the planet at the beginning and the end of each exposure, and for each surface element compute the fraction of the exposure for which that surface element is obscured by the planet. For each surface element, the out-of-transit line profile is diminished by the line profile contribution from that surface element, multiplied by the fraction of the exposure for which that surface element is covered by the planet. Finally, each line profile is convolved with a model instrumental point spread function appropriate for whichever instrument took the given data.

The steps outlined above are applicable for computing a model for an arbitrary transiting planet. However, for Kepler-13 b we need to take some extra care because of the presence of the binary companion Kepler-13 B. At a separation of 1" from Kepler-13 A, this companion star is close enough that its light will enter the 2" HET fiber along with that from Kepler-13 A. Our observed stellar line profiles will thus contain components from both Kepler-13 A and B. An additional complication is that Kepler-13 B is orbited by a stellar companion, Kepler-13 Bb, and

thus exhibits radial velocity variations. I use the orbital elements for Kepler-13 Bb presented by Santerne et al. (2012) to calculate the velocity of Kepler-13 B at each exposure. I then compute an analytic rotationally broadened line profile for Kepler-13 B, Doppler shift it and scale it relative to the Kepler-13 A profile, and add it to the line profile for Kepler-13 A. Including this profile and the resulting dilution of the spectroscopic transit signature is necessary to accurately model the data.

Fitting to the model is again accomplished using the methods of Markwardt (2009), specifically the IDL functions MPFITFUN and MPFITFUN2D. I fit for the parameters sequentially. First, I fit to the time series line profiles, and extract $v \sin i$. Then, the average line profile is subtracted off, and I simultaneously fit λ and b, leaving the planet-star radius ratio fixed at the literature value. Finally, I fit R_p/R_*, leaving all of the other parameters fixed.

The code of Markwardt (2009) provides a covariance matrix for the fit parameters from which I can calculate formal errors. However, given the small error bars produced by this code and the relatively low signal-to-noise of my data, I suspect that these errors are not trustworthy. Nonetheless, I will quote these errors below as I do not currently have any other way to compute errors on the extracted transit parameters. I am currently working on constructing a more robust error estimation code, for instance a Markov chain Monte Carlo (MCMC).

2.4 Testing the Code

In order to verify that the code is working correctly, I performed a number of tests. First, I used one of the Doppler tomographic datasets on WASP-33 b, presented by Collier Cameron et al. (2010b), taken using the 2.7m HJST at McDonald Observatory. I am able to reproduce their results (Figs. 2.1 and 2.2), an important test of my code; indeed, careful inspection suggests that the noise floor achieved by my code is somewhat lower than that of the previous work.

Another test is to observe a transit of a planet that has previously been observed via traditional Rossiter-McLaughlin observations, and check that we obtain the same results. Consequently, we observed a transit of HAT-P-2 b on 2012 June 27 UT, again using the 2.7m telescope at McDonald. Albrecht et al. (2012) determined that the spin-orbit misalignment of this planet is $\lambda = 9 \pm 10^{\circ}$. The results are shown in Fig. 2.3. I have not yet quantitatively analyzed the data given the large systematics obvious in Fig. 2.3; however, the transit signature is qualitatively consistent with what we would expect given the previously-determined system parameters (i.e., a prograde, low-inclination orbit).

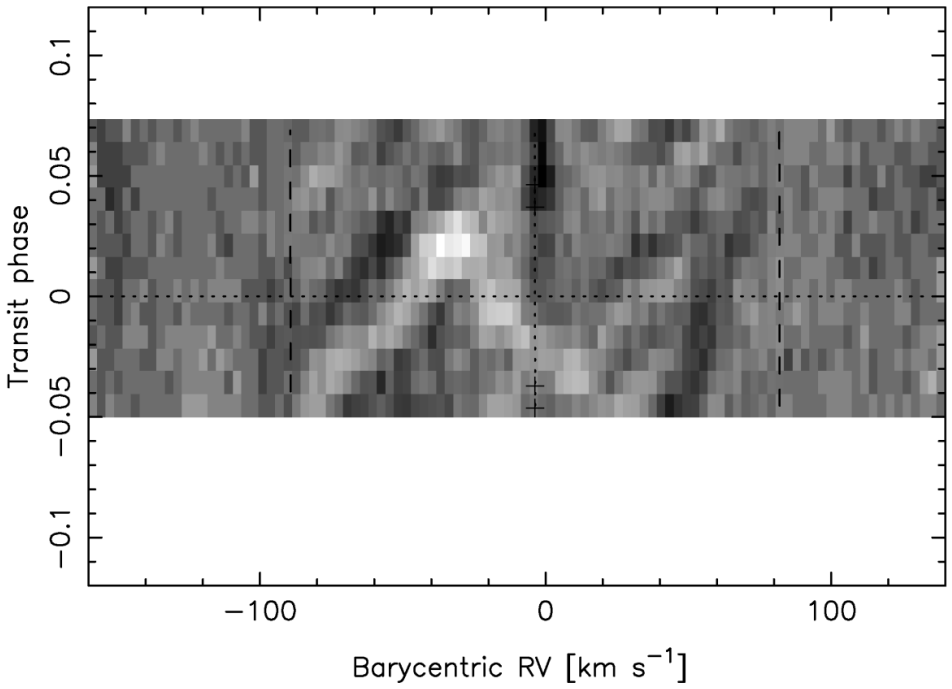

Figure 2.1 Time series line profile residuals of a transit of WASP-33 b, as presented by Collier Cameron et al. (2010b) (Fig. 4 of that work). Time increases from bottom to top. The transit signature is the bright streak moving from bottom center to upper left, while the pattern of alternating dark and light streaks moving from lower left to upper right are non-radial oscillations of the host star WASP-33 (the star is a δ Scuti variable; Herrero et al. 2011). Vertical lines mark $v = 0, \pm v \sin i$, and a horizontal dashed line marks the time of mid-transit. Small crosses mark the times of first, second, third and fourth contacts.

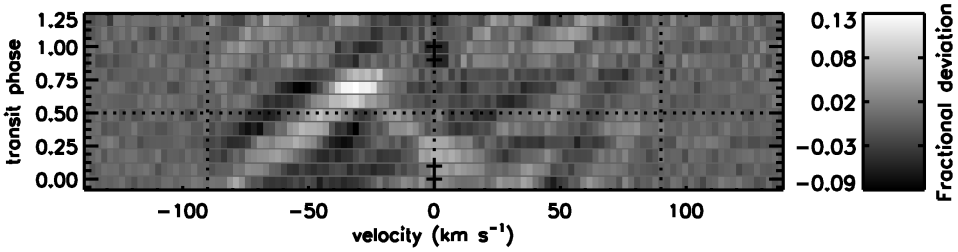

Figure 2.2 Same as Fig. 2.1, but using my own code.

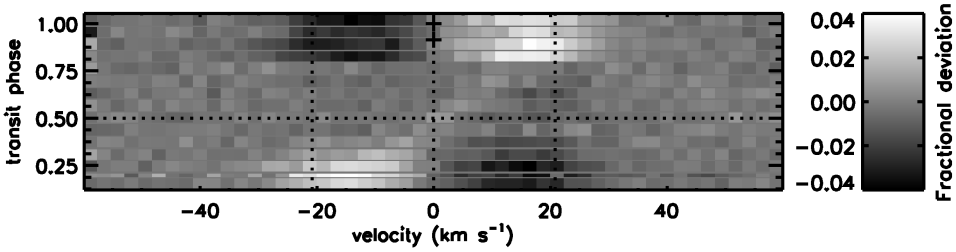

Figure 2.3 Transit of HAT-P-2 b, observed with the 2.7m Harlan J. Smith Telescope on 2012 June 27 UT. The transit signature is the bright streak moving from lower left to upper right. Significant systematics still exist in the time series line profile residuals for this relatively narrow-lined star ($v \sin i$ = 20.8 km s^{-1}), which I am working to mitigate or eliminate entirely. Notation on the figure is the same as on Fig. 2.1.

Chapter 3

Results

In Figs. 3.1, 3.2, and 3.3 we show our extracted time series line profile residuals for Kepler-13 b from HET data. The transit signature is immediately visually apparent.

As noted in Chapter 2.3, the error bars that I quote below are not trustworthy but my Markov chain Monte Carlo code is still under construction, so I do not have any other way to estimate the errors at the current time. I find a best-fit spin-orbit misalignment of $\lambda = -21.3 \pm 0.2^\circ$, in agreement with the value of $\lambda = -24^\circ \pm 4^\circ$ found by Barnes et al. (2011). I also find $b = 0.772 \pm 0.002$. In Fig. 3.4 I show the time series line profile residuals with the best-fit model, using these parameters, subtracted off.

In comparing my value for b with the literature, it is striking that there is a large degree of disagreement between the published values: $b = 0.253 \pm 0.020$ (Szabó et al. 2012), $b = 0.32$ (Barnes et al. 2011), $b = 0.3681^{+0.0041}_{-0.0064}$ (Esteves et al. 2013),

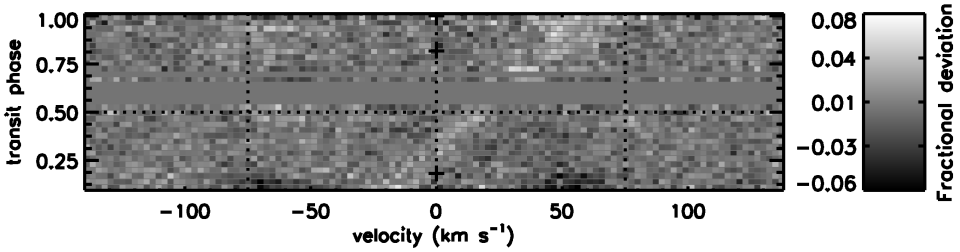

Figure 3.1 Transit signature of Kepler-13 b; the transit signature is the bright streak moving from bottom center to upper right. All data are from the HET; the upper block is from the transit of 2011 June 8 UT, the lower from 2011 July 8. Notation on the figure is the same as on Fig. 2.1.

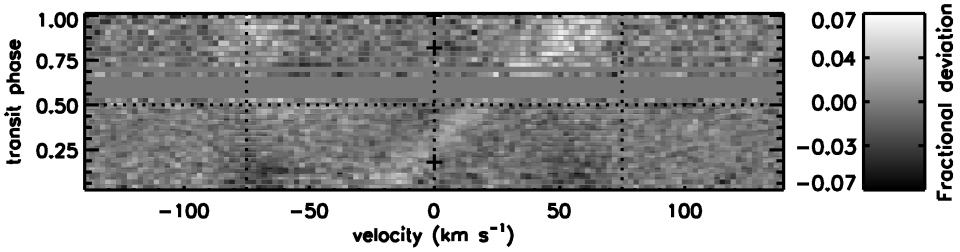

Figure 3.2 Transit signature of Kepler-13 b, using the best quality HET data. The upper block is from the transit of 2011 June 8 UT, the lower from 2011 July 6 and 8. Notation on the figure is the same as on Fig. 2.1.

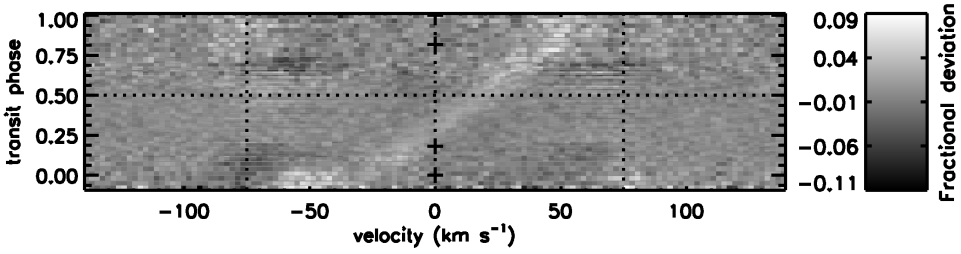

Figure 3.3 Transit signature of Kepler-13 b, using all of our HET data. Notation on the figure is the same as on Fig. 2.1.

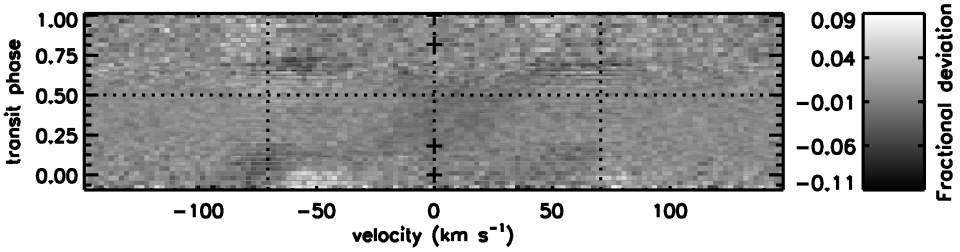

Figure 3.4 Same as Fig. 3.3, but with the best-fitting transit model subtracted. The transit signature is well-subtracted but there are still significant systematic residuals. Notation on the figure is the same as on Fig. 2.1.

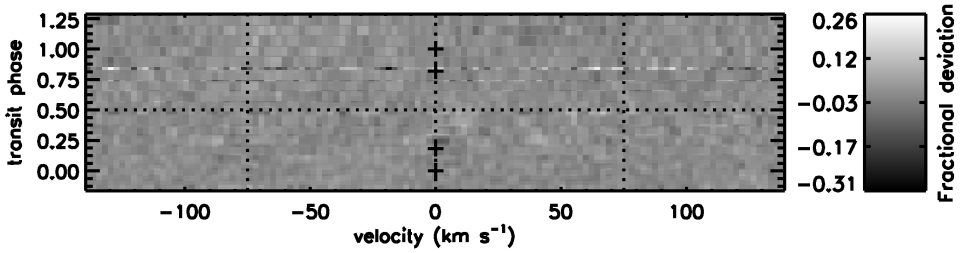

Figure 3.5 Transit data on Kepler-13 b from the HJST, using data from both observed transits. A small bright spot at low positive velocities just before mid-transit is consistant with the transit, but the signal-to-noise level is so low that this is likely noise; compare full range of the grayscale scale bar to that for the HET data. Notation on the figure is the same as on Fig. 2.1.

and $b = 0.75 \pm 0.01$ (Mazeh et al. 2012). Work is currently in progress on code to fit the *Kepler* photometry simultaneously with the time series line profile residuals, which may clarify this issue.

We also observed two transits of Kepler-13 b using the HJST. These data are shown in Figs. 3.5 and 3.6. Unlike for the HET data, the transit signature is not visually apparent.

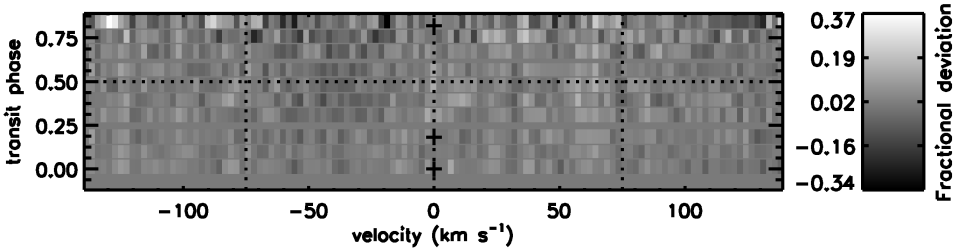

Figure 3.6 Same as Fig. 3.5, except using only the HJST data from 2011 November 5 UT. Notation on the figure is the same as on Fig. 2.1.

Chapter 4

Discussion

As a hot Jupiter in a multiple stellar system, it is plausible that Kepler-13 b could have been emplaced on its current orbit through Kozai cycles followed by tidal damping. As it possesses a significantly non-zero spin-orbit misalignment, it could alternatively been emplaced on its current orbit by planet-planet scattering or migration within an inclined disk (Batygin 2012), or the stellar spin may have changed through the mechanism proposed by Rogers et al. (2012). While any of these processes could be responsible for the inclined orbit of Kepler-13 b, it is difficult to assign responsibility for any given planetary system; measurements of the spin-orbit misalignments of many planets are necessary to statistically disentangle different migration scenarios. I will, however, briefly consider migration via Kozai cycles in particular, and whether there is at present any evidence for differences in the spin-orbit misalignment statistics for planets in multiple systems versus planets orbiting

stars with no additional companions.

In order to investigate this, I searched the literature for planets with measured values of λ, and separated these planets into four categories: those orbiting stars with known proper motion binary companions, those with suspected companions not yet confirmed with proper motions, those with either a radial velocity trend indicating the presence of an additional long-period companion or a known exterior planet, and those exhibiting no signs of additional bodies in the system. I will hereafter collectively refer to stars in the first two categories as "binary systems," and those in the last category as "single systems." For much of the analysis, I will neglect those systems with suspected binary companions, as it is not clear into which category these should fit, and there are moreover only a small number of such systems ($N = 3$, compared to 42 single systems and 15 binary systems; one of these, however, is WASP-33, which does have a radial velocity trend, so it is also included in the binary sample). I do not include in the sample compact multiplanet systems; all of these that have been observed to date are well-aligned (Albrecht et al. 2013b), consistent with evolution through only disk migration, and thus appear to be a population distinct from hot Jupiters. I do include my measurement of the spin-orbit misalignment of Kepler-13 b presented in this work in this dataset.

In Fig. 4.1 I show the distribution of $|\lambda|$ as a function of T_{eff}, like Winn et al. (2010) and Albrecht et al. (2012), but with the points color-coded according to

binarity status. While the number of known binary systems is small, it is noteworthy that the two retrograde planets around cool stars, WASP-8 b and HAT-P-11 b, both exist in systems with a known proper motion companion and/or a radial velocity trend. These were noted by Winn et al. (2010) and Albrecht et al. (2012) as outliers in the trend of planets around cooler stars being preferentially aligned; they also noted that both of these planets should have long tidal damping timescales–WASP-8 b because it has a relatively long period ($P = 8.2$ days) and HAT-P-11 b because it has a small mass ($M = 0.083 M_J$). Thus, it is possible that these planets are misaligned because of Kozai cycles, and maintain that misalignment due to the long tidal damping timescales.

I will now quantitatively consider the distributions of $|\lambda|$ for these different populations, and attempt to determine whether or not they are drawn from the same underlying distribution. In Fig. 4.2 I show the cumulative distributions of $|\lambda|$ for planets in single and binary systems around cool and hot stars. I performed two-sided KS tests on these distributions. These indicated a 47% probability that the planets around cool single and binary stars are drawn from the same distribution, and a 55% probability that the planets around hot single and binary stars are drawn from the same distribution. These results support the null hypothesis that the distributions of $|\lambda|$ for binary systems and single systems is the same.

I note, however, that due to the very small sample size for the binary systems

($N_{cool} = 9, N_{hot} = 6$), more data are needed in order to be able to draw any statistically significant conclusions. My work will help to expand this sample; I have in hand, but have not yet reduced and analyzed, data on two transits of another hot Jupiter orbiting one member of a binary star system. The sample can also be increased by a systematic search of known planet hosts for proper motion companions, such as that being undertaken by Narita et al. (2012). There are also a handful of other systems with known binary companions or radial velocity trends for which no spin-orbit misalignment measurements exist. The most favorable of these targets is WASP-77 A b, with $v \sin i = 4.0$ km s^{-1} and $T_{eff} = 5500$ K. Other possible but less favorable targets include WASP-34 b ($v \sin i = 1.4$ km s^{-1}) and CoRoT-1 b ($v \sin i = 5.2$ km s^{-1}). The latter system was observed using Rossiter-McLaughlin observations by Pont et al. (2010), but due to the low signal-to-noise (the star is faint, at $V = 13.6$) this measurement is not included in our analysis or those of Winn et al. (2010) or Albrecht et al. (2012). As noted by Albrecht et al. (2012), however, this would be an interesting system to reobserve as it orbits a cool star and the value of $\lambda = 77 \pm 11^\circ$ found by Pont et al. (2010), if confirmed, would add to the number of cool stars with misaligned planets.

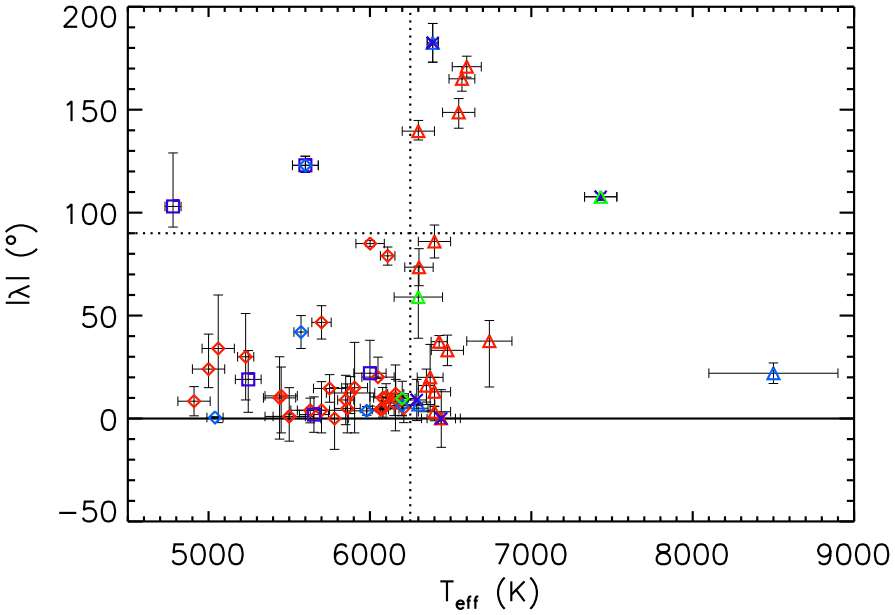

Figure 4.1 Distribution of $|\lambda|$ versus stellar effective temperature for all stars in our literature sample, plus Kepler-13 b. Blue points denote systems with proper motion companions, green systems with suspected companions not yet confirmed via proper motion, purple systems with radial velocity trends (some overlap with the previous two categories), and red stars exhibiting none of these features. Diamonds and squares denote stars with $T_{eff} < 6250$ K, while traingles and Xs denote those with $T_{eff} \geq 6250$ K. Horizontal lines denote $|\lambda| = 0°$ (solid) and $|\lambda| = 90°$ (dotted), while a dotted vertical line marks $T_{eff} = 6250$ K.

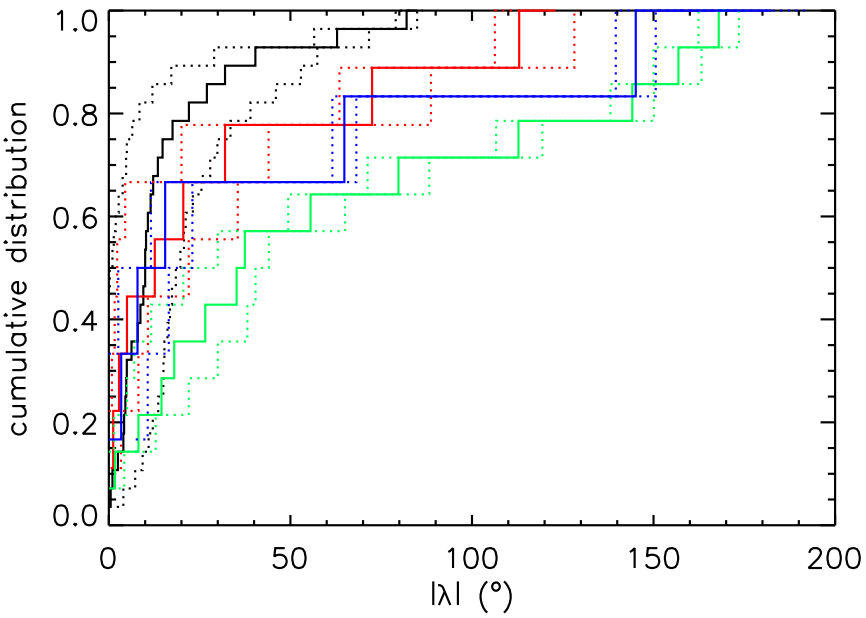

Figure 4.2 Cumulative distributions of $|\lambda|$ for planets around single cool (black) and hot (green) stars, and stars with known binary companions or radial velocity trends that are cool (red) or hot (blue). 1σ limits on each value of $|\lambda|$ are shown as dotted lines in the same color as each solid line.

Chapter 5

Conclusions

I have constructed a Doppler tomography code which now rivals previously established codes in terms of precision. I have validated this code by analyzing data on transits of WASP-33 b and HAT-P-2 b.

I have presented Doppler tomographic observations for the *Kepler* planet Kepler-13 b, confirming the spin-orbit misalignment found by Barnes et al. (2011) and breaking the degeneracy in their gravity darkening-based measurements, showing that the planetary orbit is prograde.

Kepler-13 b is a hot Jupiter, and thus the measurement of the spin-orbit misalignment does not directly address the questions discussed in Chapter 1, as it has a short orbital period and does not inhabit a compact multiplanet system. The measurement of its spin-orbit misalignment, however, does contribute to answering the questions posed in Chapter 1, in a different manner. Kepler-13 is by far the

hottest planet host star for which the spin-orbit misalignment has been measured. With the exception of WASP-33 b, all of the other planets for which the spin-orbit misalignment has been measured (and from which the two distributions noted by Winn et al. (2010) are seen) have host stars with $T_{eff} < 7000$ K, corresponding to stellar masses of $M_* \lesssim 1.5 M_\odot$ on the main sequence. While the trend of a wide distribution of spin-orbit misalignments is expected to continue for even hotter, more massive stars, it is important to observationally verify whether this is correct. While there are currently only two data points with $T_{eff} > 7000$ K, both show a statistically significant degree of misalignment, suggesting that these hotter stars do indeed continue the trend seen in stars with 6250 K $< T_{eff} <$ 7000 K. In addition, Kepler-13 is a valuable measurement of a spin-orbit misalignment in a stellar multiple system, which, as discussed in Chapter 4, is a valuable tool for disentangling what, if any, contribution Kozai cycles have made to the population of hot Jupiters.

5.1 Future Work

Construction of the line profile extraction code is now essentially complete, as shown by my detection of the transits of Kepler-13 b, WASP-33 b, and HAT-P-2 b. The fitting code is working but its functionality can be improved, which is the most pressing item of current work. Now that the majority of the coding is complete,

attention can be turned to data on other systems that we have collected.

We have in hand data on numerous transits of several other systems. These comprise four *Kepler* candidates, all of which have $P > 10$ days and one of which is also located in a compact multiplanet system, and two hot Jupiters located by ground-based transiting suveys. These data will allow confirmation of these planet candidates, and expand the number and parameter space coverage of planets with spin-orbit misalignment measurements. The measurements of spin-orbit misalignments will help to address the issues discussd by Winn et al. (2010), Rogers et al. (2012), Batygin (2012), and Dawson & Murray-Clay (2013). One of our systems will be the first compact multiplanet system around a hot star with a measurement of the spin-orbit misalignment. One of the the hot Jupiters found by a ground-based survey is located in a stellar multiple system, expanding the currently small sample of planets in multiple systems with spin-orbit misalignment measurements, the importance of which is noted in Chapter 4.

The HET is expected to be out of operations for approximately six months beginning in August 2013 in order for work to be performed on upgrades to the telescope for the Hobby-Eberly Telescope Dark Energy Experiment (HETDEX). These upgrades will include improved throughput to the HRS, which will improve the prospects for this work, allowing us to achieve higher time resolution and/or push to fainter target stars or smaller planets.

While I have not yet detected the transits of any of my other *Kepler* targets (I have only reduced a subset of the data for two of the planet candidates mentioned above), I note that for the star KOI-972, a known δ Scuti variable, I have made a marginal detection of non-radial stellar oscillations (similar to those seen in WASP-33, Figs. 2.1 and 2.2); these are shown in Fig. 5.1. Use of Doppler tomography to image non-radial oscillations of pulsating stars has a long history, going back to Gies & Kullavanijaya (1988); incidentally, the observations used by these authors were obtained using the HJST. Although it is not the focus of this project, my line profile extraction code could certainly be used to image such non-radial oscillations. I also note that KOI-972 is a particularly important target, as in addition to our Doppler tomography target, KOI-972.01 ($P = 13.1$ days, $R = 6.1 R_{\oplus}$), *Kepler* data have recently allowed the discovery of a second planet candidate in the system, KOI-972.02 ($P = 7.82$ days, $R = 1.73 R_{\oplus}$). This is thus a compact multiplanet system around a hot star ($T_{eff} = 7500$ K), important for testing the hypothesis of Rogers et al. (2012) and Rogers & Lin (2013) discussed earlier.

There are a number of possible avenues for expansion of these project. While hot stars tend to be rapidly rotating, young cooler stars also rotate rapidly. These stars are often heavily spotted. The Doppler tomography technique was originally developed to map the distributions of starspots on such stars (Vogt & Penrod 1983). One of the observables for such observations is the angle between the star's spin axis

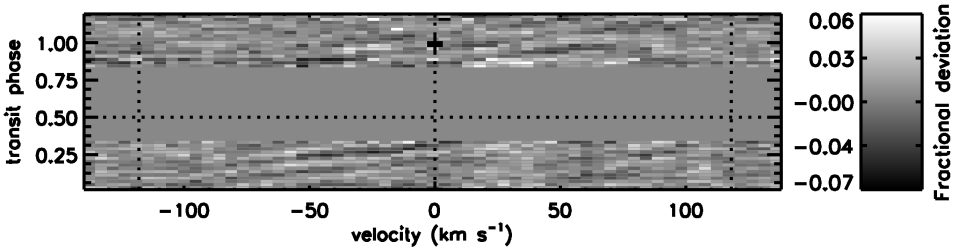

Figure 5.1 Time series line profile residuals for KOI-972, showing evidence for non-radial oscillations (faint striations running from lower left to upper right). All data are from the HET; the upper block is from the transit of 2011 August 3 UT, and the lower block from that of 2011 August 16. Notation on the figure is the same as for Fig. 2.1. The planetary transit is not visible in these data.

and the line of sight. The spin-orbit misalignment derived from our observations of hot stars is not the full three-dimensional spin-orbit misalignment, but rather this misalignment projected on the plane of the sky. Thus, Doppler tomographic observations of a transiting planet around a young, rapidly rotating, spotted star would allow a measurement of the full three-dimensional spin-orbit misalignment by combing observations of the spots and the transiting planet. Moreoever, this is one of the only techniques that can confirm planets around such stars, where radial velocity jitter due to starspots is a significant problem. Such planets would also be younger than the tidal realignment timescale of the system, allowing a direct probe of the Winn et al. (2010) hypothesis that the low obliquities of planets around cool stars is a consequence of tidal realignment of an initially misaligned population. Currently the only known transiting planet candidate around a young, spotted star, the T Tauri star PTFO 8-8695 (van Eyken et al. 2012), is too faint, at $V \sim 16$,

for Doppler tomographic observations with current facilities. We will work with transiting planet surveys to identify suitable candidates for this type of observation.

5.2 Sensitivity Estimation

Another question to consider is what sensitivity I could expect to obtain from a given number of observations of a star of a given magnitude. In particular, in concert with the upcoming HETDEX upgrades to the HET, upgrades to HRS will increase the throughput by a factor of ~ 2.3 (P. J. MacQueen, private communication). Doppler tomography is potentially a powerful technique for validating planets too small for the radial velocity variations of the host star to be detected; how small a planet could we detect with a reasonable amount of observing time?

In order to answer this question, I take the following approach. I assume that the line profile derived from my code can be approximated mathematically by simply taking an average of all sufficiently strong lines ("sufficiently strong" to be defined empirically by considering datasets with detected transits).

The signal-to-noise ratio of a single line will be

$$SNR_{line} = SNR_{cont} \times d \times f \tag{5.1}$$

where SNR_{line} and SNR_{cont} are the signal-to-noise ratios of the line and the continuum, respectively, d is the depth of the line for $v \sin i = 0$, and f is the factor

by which the depth is diminished by line broadening. From Gray (2005), an analytic formula for a rotationally broadened stellar line shape, assuming a linear limb darkening law, is

$$G(v) = c_1[1 - (v/v\sin i)^2]^{1/2} + c_2[1 - (v/v\sin i)^2] \tag{5.2}$$

where $G(v)$ is the shape of the profile in velocity space, and the constants c_1 and c_2 are

$$c_1 = \frac{2(1-\epsilon)}{\pi v \sin i(1-\epsilon/3)},\ c_2 = \frac{1}{2}\frac{\epsilon}{v\sin i(1-\epsilon/3)} \tag{5.3}$$

where ϵ is the linear limb darkening parameter. Thus, $c_1, c_2 \propto 1/v\sin i$. Now, it is apparent that, at the center of the line profile ($v = 0$), $G(v) = c_1 + c_2$. Since c_1, c_2 diverge as $v \to 0$, I will make the assumption that the depths are equal to the baseline depth from VALD for a star with $v\sin i \sim \xi \sim 2$ km s^{-1}, where ξ is the microturbulent velocity. Thus, I have $f = 2$ km s$^{-1}/v\sin i$. Now, the signal-to-noise ratio of the continuum in a normalized spectrum is $SNR_{cont} = 1/\sigma$, where σ is the error in the continuum. Thus, we can write

$$SNR_{line} = \frac{2d}{\sigma v\sin i} \tag{5.4}$$

where $v\sin i$ is in km s^{-1}.

Now, we wish to consider an ensemble of lines, each with its own depth

$d_i = df$ and error σ_i. Each will have the line profile $G(v)_i = G(v)d_i$, and the normalized line profile will be $G(v)_i/d_i = G(v)$. Thus, the average line profile for M lines will be, normalizing the profiles before averaging,

$$G(v)_{tot} = \frac{1}{M}\sum_{i=1}^{M}\frac{G(v)_i d_i}{d_i} = \frac{1}{M}\sum_{i=1}^{M} G(v)_i \tag{5.5}$$

Therefore, the error on any one pixel in the average line profile will be

$$\sigma_{tot}^2 = \left(\frac{1}{M}\right)^2 \sum_{i=1}^{M}\frac{\sigma_i^2}{d_i^2} = \frac{1}{M^2}\sum_{i=1}^{M}\frac{1}{SNR_{line,i}^2} \tag{5.6}$$

For a given star, we can obtain line depths from a line list and model atmosphere calculation (e.g., from VALD). One approach is to use a signal-to-noise calculation tool, such as are provided by many observatories,[1] to calculate SNR_{cont}. Alternatively, by assuming that, for a given pixel in the raw spectrum, the errors are simple $\sqrt{N}$ photon counting error, we can estimate how many photons we need to collect in order to obtain a given error level in the average line profile. If we collect N photons in a continuum pixel, the error will be $\sigma = \sqrt{N}$. If we then normalize the spectrum, the error on this pixel with be $\sigma = \sqrt{N}/N = N^{-1/2}$. So, we can rewrite

[1] e.g., http://het.as.utexas.edu/HET/hetweb/Instruments/HRS/exp/exp_calc.html for the HET/HRS,
http://etc.ucolick.org/web_s2n/hires for Keck/HIRES

Eqn. 5.6 as

$$\sigma_{tot}^2 = \frac{1}{M^2} \sum_{i=1}^{M} \frac{1}{N_i d_i^2} \tag{5.7}$$

where N_i is the number of photons per pixel in the continuum adjacent to line i. As a final simplifying assumption, let us assume that we have M identical lines, each with depth d and N photons per pixel. We will thus have

$$\sigma_{tot}^2 = \frac{M}{NM^2d^2} \tag{5.8}$$

so

$$\sigma_{tot}^2 = \frac{1}{MNd^2} \tag{5.9}$$

If we instead take a weighted average of the lines (weighting by d_i), the results for an ensemble of M identical lines will be the same, but the general case (Eqns. 5.5 and 5.7) will be

$$G(v)_{tot} = \sum_{i=1}^{M} \frac{G(v)_i d_i d_i}{d_i} / \sum_{i=1}^{M} d_i = \sum_{i=1}^{M} G(v)_i d_i / \sum_{i=1}^{M} d_i \tag{5.10}$$

$$\sigma_{tot}^2 = \sum_{i=1}^{M} \frac{d_i^2}{N_i d_i^2} / \left(\sum_{i=1}^{M} d_i \right)^2 = \sum_{i=1}^{M} \frac{1}{N_i} / \left(\sum_{i=1}^{M} d_i \right)^2 \tag{5.11}$$

Now that we have expressions for the expected noise level, I need to consider what noise level would be needed to detect a given planet. For the time being I shall use the following approach. I will first compute a model transit signature

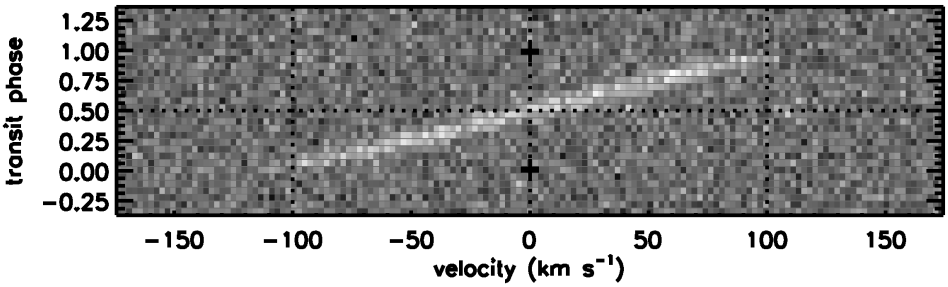

Figure 5.2 Time series line profile residuals a transit of a planet with $R_p/R_* = 0.02$ around a star with $v \sin i = 100$ km s^{-1}. The planet has $\lambda = 0°$ and $b = 0$. The noise level is $\sigma = 0.001$, the detection limit for this set of parameters from Table 5.1. Notation on the figure is the same as for Fig. 2.1.

using the model described in Chapter 2.3, and then to each pixel in the resulting time series line profile residual maps I will add a random number drawn from a Gaussian distribution with mean zero and width σ_{tot}. I am thus assuming white noise at a level consistent with the estimates derived above. I then lower σ until the transit signature is visually apparent. Obviously this also neglects the fact that the noise will be slightly larger within the line profile than outside the line profile because of the lower flux within the line. Finding a quantitative way to determine whether or not a transit has been detected is an item of future work. I do this for a representative sample of planetary and stellar parameters, summarized in Table 5.1. I assume a baseline period of 5 days, and exposure length of 600 seconds. A representative example of a simulated time series line profile residual map is shown in Fig. 5.2

Now, we need to know how many photons the HET collects in a given period

of time. We get the best signal-to-noise and have the most lines in the region $\sim 5000 - 6000$ Å, so I will use the V-band flux to estimate the photon count. From Bessell et al. (1998), the V-band flux from a zeroth-magnitude A0 star (i.e. Vega) is $F_\lambda = 3.631 \times 10^{-9}$ ergs cm^{-2} s^{-1} Å^{-1}. Assuming that 75% of the HET mirror is illuminated, on average, during a track, and using a HRS throughput of 1.2%[2] multiplied by the 2.3× improvement from the upcoming HRS upgrades, I calculate the number N of photons measured in each pixel in wavelength space. I use this to calculate σ_{tot} using Eqn. 5.9, assuming $M = 500$ lines of average depth $d = 0.05$. I assume n visits, each with an exposure length of 600 seconds, and increase n until σ_{tot} is equal to the value of σ for a given planet/star combination estimated earlier. n is the number of times we must observe a given part of the transit in order to detect the planet. I perform this analysis for a $V = 11$ star, typical of *Kepler* targets, and a $V = 8$ star, representing the most favorable *Kepler* targets or targets from other surveys. The results are summarized in Table 5.1. I note that these figures are not intended to be rigorous predictions, but rather order-of-magnitude estimates for the feasibility of observing a given class of target. A more rigorous analysis, using the full Eqn. 5.6 and 5.11, will have to be performed for any given target.

It is immediately apparent that the necessary number of visits, and therefore exposure time, in order to detect a given planet is, in some cases, highly unreason-

[2] http://hydra.as.utexas.edu/?a=help&h=37

Table 5.1. Estimated Sensitivity Levels

R_p/R_*	$v \sin i$ (km s^{-1})	σ_{max}	Visits ($V = 11$)	Visits ($V = 8$)
0.1	50	0.01	1	1
0.1	100	0.02	1	1
0.05	50	0.003	8	1
0.05	100	0.006	3	1
0.02	50	5×10^{-4}	325	22
0.02	100	0.001	75	5
0.01	50	2.5×10^{-4}	1250	80
0.01	100	5×10^{-4}	325	22
0.005	50	1×10^{-4}	7500	100
0.005	100	2.5×10^{-4}	1250	80

able. For instance, we could detect a planet with $R_p/R_* = 0.01$, corresponding to a $1R_\oplus$ planet around a $1R_\odot$ star, or a $2R_\oplus$ planet around a $2R_\odot$ star, with 325 visits for $v \sin i = 100$ km s^{-1}. For a fairly typical three hour long transit this would represent about 1000 hours of telescope time, an unreasonable allotment. Furthermore, for a planet with a period of 5 days, even if every transit was observed (which is not possible due to daylight, weather, etc.), it would take nearly five years to observe the necessary number of transits. This is clearly not feasible.

Prospects are considerably brighter for brighter stars. I find that a planet with $R_p/R_* = 0.02$, corresponding to a $2R_\oplus$ planet around a $1R_\odot$ star (i.e., a super-Earth), or a $4R_\oplus$ planet around a $2R_\odot$ star, could be detected in a mere 5 visits for a $V = 8$ star, corresponding to a mere ~ 15 hours of observing time, a much more

reasonable allocation. Thus, I conclude that while small planets remain out of our reach around faint stars, should any favorable candidates be found around bright stars we have good prospects for detection of the transits. I also note that, qualitatively, the σ necessary in order to detect a transit scales as roughly $\sigma \propto 1/v \sin i$, so prospects are also better for even more rapidly rotating stars. Conversely, more slowly rotating, cooler stars will have more deep lines, increasing M and d; I note that $\sigma \propto N^{-1/2} d^{-1}$. A more thorough, quantitative exploration of our detection limits is an item of future work. I suggest that future transit surveys, such as the recently-selected NASA mission TESS (e.g., Deming et al. 2009) should consider observing rapidly-rotating stars, for which we will be able to validate small planets.

Bibliography

Aitken, R. G. 1904, Lick Observatory Bulletin, 3, 6

Albrecht, S., Setiawan, J., Torres, G., Fabrycky, D. C., & Winn, J. N. 2013a, ApJ, 767, 32

Albrecht, S., Winn, J. N., Johnson, J. A., et al. 2012, ApJ, 757, 18

Albrecht, S., Winn, J. N., Marcy, G. W., et al. 2013b, ApJ, 771, 11

Asplund, M., Grevesse, N., Sauval, A. J., & Scott, P. 2009, ARA&A, 47, 481

Barnes, J. W. 2009, ApJ, 705, 683

Barnes, J. W., Linscott, E., & Shporer, A. 2011, ApJS, 197, 10

Batygin, K. 2012, Nature, 491, 418

Bessell, M. S., Castelli, F., & Plez, B. 1998, A&A, 333, 231

Bodenheimer, P., Hubickyj, O., & Lissauer, J. J. 2000, Icarus, 143, 2

Brown, D. J. A., Collier Cameron, A., Díaz, R. F., et al. 2012, ApJ, 760, 139

Carson, J., Thalmann, C., Janson, M., et al. 2013, ApJL, 763, L32

Collier Cameron, A., Bruce, V. A., Miller, G. R. M., Triaud, A. H. M. J., & Queloz, D. 2010a, MNRAS, 403, 151

Collier Cameron, A., Guenther, E., Smalley, B., et al. 2010b, MNRAS, 407, 507

Dawson, R. I. & Murray-Clay, R. A. 2013, ApJL, 767, L24

Deming, D., Seager, S., Winn, J., et al. 2009, PASP, 121, 952

Donati, J.-F., Semel, M., Carter, B. D., Rees, D. E., & Collier Cameron, A. 1997, MNRAS, 291, 658

Esteves, L. J., De Mooij, E. J. W., & Jayawardhana, R. 2013, arXiv:1305.3271

Fabrycky, D. & Tremaine, S. 2007, ApJ, 669, 1298

Fischer, D. A. & Valenti, J. 2005, ApJ, 622, 1102

Gandolfi, D., Collier Cameron, A., Endl, M., et al. 2012, A&A, 543, L5

Gies, D. R. & Kullavanijaya, A. 1988, ApJ, 326, 813

Goldreich, P. & Tremaine, S. 1980, ApJ, 241, 425

Gray, D. F. 2005, The Observation and Analysis of Stellar Photospheres, 3rd edn. (Cambridge: Cambridge University Press)

Herrero, E., Morales, J. C., Ribas, I., & Naves, R. 2011, A&A, 526, L10

Kaib, N. A., Raymond, S. N., & Duncan, M. J. 2011, ApJL, 742, L24

Kley, W. & Nelson, R. P. 2012, ARA&A, 50, 211

Kupka, F. G., Ryabchikova, T. A., Piskunov, N. E., Stempels, H. C., & Weiss, W. W. 2000, Baltic Astronomy, 9, 590

Lin, D. N. C., Bodenheimer, P., & Richardson, D. C. 1996, Nature, 380, 606

Markwardt, C. B. 2009, in Astronomical Society of the Pacific Conference Series, Vol. 411, Astronomical Data Analysis Software and Systems XVIII, ed. D. A. Bohlender, D. Durand, & P. Dowler, 251

Mayor, M. & Queloz, D. 1995, Nature, 378, 355

Mazeh, T., Nachmani, G., Sokol, G., Faigler, S., & Zucker, S. 2012, A&A, 541, A56

McLaughlin, D. B. 1924, ApJ, 60, 22

Miller, G. R. M., Collier Cameron, A., Simpson, E. K., et al. 2010, A&A, 523, A52

Mislis, D. & Hodgkin, S. 2012, MNRAS, 422, 1512

Narita, N., Takahashi, Y. H., Kuzuhara, M., et al. 2012, PASJ, 64, L7

Pont, F., Endl, M., Cochran, W. D., et al. 2010, MNRAS, 402, L1

Rasio, F. A. & Ford, E. B. 1996, Science, 274, 954

Rogers, T. M. & Lin, D. N. C. 2013, ApJL, 769, L10

Rogers, T. M., Lin, D. N. C., & Lau, H. H. B. 2012, ApJL, 758, L6

Rossiter, R. A. 1924, ApJ, 60, 15

Santerne, A., Moutou, C., Barros, S. C. C., et al. 2012, A&A, 544, L12

Shporer, A., Jenkins, J. M., Rowe, J. F., et al. 2011, AJ, 142, 195

Sneden, C., Bean, J., Ivans, I., Lucatello, S., & Sobeck, J. 2012, MOOG: LTE line analysis and spectrum synthesis, astrophysics Source Code Library

Struve, O. 1952, The Observatory, 72, 199

Szabó, G. M., Pál, A., Derekas, A., et al. 2012, MNRAS, 421, L122

Szabó, G. M., Szabó, R., Benkő, J. M., et al. 2011, ApJL, 736, L4

Triaud, A. H. M. J., Collier Cameron, A., Queloz, D., et al. 2010, A&A, 524, A25

Tull, R. G. 1998, in Society of Photo-Optical Instrumentation Engineers (SPIE) Conference Series, Vol. 3355, Society of Photo-Optical Instrumentation Engineers (SPIE) Conference Series, ed. S. D'Odorico, 387–398

van Eyken, J. C., Ciardi, D. R., von Braun, K., et al. 2012, ApJ, 755, 42

Vogt, S. S. & Penrod, G. D. 1983, PASP, 95, 565

Winn, J. N., Fabrycky, D., Albrecht, S., & Johnson, J. A. 2010, ApJL, 718, L145

Winn, J. N., Howard, A. W., Johnson, J. A., et al. 2011, AJ, 141, 63

Wright, J. T., Marcy, G. W., Howard, A. W., et al. 2012, ApJ, 753, 160